Published in final edited form as:
J Biomech. 2014 March 3; 47(4): 870–877. doi:10.1016/j.jbiomech.2014.01.010.

Effect of tissue properties, shape and orientation of microcalcifications on vulnerable cap stability using different hyperelastic constitutive models

Luis Cardoso[1,2], **Adreanne Kelly-Arnold**[1], **Natalia Maldonado**[1], **Damien Laudier**[1], and **Sheldon Weinbaum**[1,2]

[1]Department of Biomedical Engineering, The City College of New York of The City University of New York, New York, USA

[2]The Graduate Center of The City University of New York, New York, NY, USA

Abstract

Approximately half of all cardiovascular deaths associated with acute coronary syndrome occur when the thin fibrous cap tissue overlying the necrotic core in a coronary vessel is torn, ripped or fissured under the action of high blood pressure. From a biomechanics point of view, the rupture of an atheroma is due to increased mechanical stresses in the lesion, in which the ultimate stress (i.e. peak circumferential stress (PCS) at failure) of the tissue is exceeded. Several factors including the cap thickness, morphology, residual stresses and tissue composition of the atheroma have been shown to affect the PCS. Also important, we recently demonstrated that microcalcifications (μCalcs) > 5 μm are a common feature in human atheroma caps, which behave as local stress concentrators, increasing the local tissue stress by at least a factor of two surpassing the ultimate stress threshold for cap tissue rupture. In the present study, we used both idealized μCalcs with spherical shape and actual μCalcs from human coronary atherosclerotic caps, to determine their effect on increasing the circumferential stress in the fibroatheroma cap using different hyperelastic constitutive models. We have found that the stress concentration factor (SCF) produced by μCalcs in the fibroatheroma cap is affected by the material tissue properties, μCalcs spacing, aspect ratio and their alignment relative to the tensile axis of the cap.

Keywords

micro computed tomography; vulnerable plaque; microcalcifications; fibrous cap rupture

Address correspondence to: Sheldon Weinbaum, PhD. The City College of The City University of New York, Steinman Hall T-404B, 140th Street and Convent Ave, New York, New York 10031 USA; 212.650.5202 (Office); 212.650.6727(Fax); Weinbaum@ccny.cuny.edu.

Conflict of interest
The authors have no conflict of interest.

INTRODUCTION

Approximately half of all cardiovascular deaths associated with acute coronary syndrome occur when the thin fibrous cap tissue overlying the necrotic core in a coronary vessel is torn, ripped or fissured under the action of high blood pressure (Davies and Thomas, 1981; Davies and Thomas, 1985; Burke et al., 1999). Based on its morphology and tissue composition, a vulnerable plaque has been described as a positively remodeled lesion rich in vasa-vasorum containing a lipid rich pool with a fibrous cap infiltrated by macrophages (Burke et al., 1997; Burke et al., 1999; Virmani et al., 2003; Virmani et al., 2007). From a biomechanics point of view, the rupture of an atheroma is due to increased mechanical stresses in the lesion, in which the ultimate stress (i.e. peak circumferential stress (PCS) at failure) of the tissue is exceeded as initially proposed in (Born and Richardson, 1989; Richardson et al., 1989). This basic hypothesis was subsequently explored by numerous investigators using 2D and 3D finite element analysis (FEA) and fluid structure interaction numerical models in which various aspects of plaque morphology, tissue properties, residual and fluid shear stress are examined (Cheng et al., 1993; Finet et al., 2004; Tang et al., 2005; Vengrenyuk et al., 2008; Akyildiz et al., 2011; Speelman et al., 2011; Rambhia et al., 2012). These and related studies are described in more detail in a recent review by Cardoso and Weinbaum (2013).

An important advance in the PCS hypothesis was the realization that cellular level microcalcifications (μCalcs) in fibrous caps could behave as local stress concentrators, increasing the local tissue stress by at least a factor of two surpassing the ultimate stress threshold for cap tissue rupture (Vengrenyuk et al., 2006). The presence of μCalcs in caps is a plausible explanation as to why approximately 40% of cap tears occur in the center of the cap (Richardson et al 1989; Maehara et al. 2002), why ruptures frequently did not coincide with the predicted location of PCS and why caps > 65 μm thickness could rupture at tissue stresses far below the 300 kPa critical threshold proposed in Cheng et al. (1993). In a series of studies (Vengrenyuk et al., 2006; Vengrenyuk et al., 2008; Vengrenyuk et al., 2010; Maldonado et al., 2012; Maldonado et al., 2013) the μCalc hypothesis has been further explored leading to the most recent paper, Kelly-Arnold et al. (2013), in which nearly 35,000 μCalcs > 5 μm were observed and analyzed in the fibrous caps of 22 non-ruptured lesions using 2.1-μm resolution μCT. In view of the numerous μCalcs that can now be seen in the fibrous caps it was no longer feasible to do 3D FEA or FSI calculations of the local tissue stress and simplifying numerical procedures were devised to quickly hone in on and quantitatively analyze which particle shapes and particle clusters are potentially dangerous. In the present study, we used both idealized μCalcs with spherical shape and actual μCalcs from human coronary atherosclerotic caps, to determine their effect on the circumferential stress in the cap of the fibroatheroma (FA). We have also investigated whether the stress concentration factor (SCF) produced by the μCalcs in the FA cap is affected by the material tissue properties, μCalc spacing, aspect ratio and their alignment relative to the tensile axis of the cap. This behavior is explored using several of the most widely used constitutive models.

MATERIALS AND METHODS

Idealized multi-layer model of fibroatheroma

The human coronary fibroatheroma was modeled as a thick walled non-linear elastic cylindrical tube consisting of three distinct layers, namely the tunica intima (I), tunica media (M) and adventitia (A) layer. The idealized model represents a 30mm long segment of the artery, and includes a 10mm long fibroatheroma at the mid portion of the vessel. The FA is characterized by an eccentric pathological thickening of the intima layer, containing a semi-annular lipid core (LC). The radius of the lumen in the healthy portion of the vessel is 1.6mm and gradually decreases to 1.0mm in the FA region. The thicknesses of the I, M, and A tissue layers are 0.2mm, 0.4mm and 0.3mm, respectively. Isometric views of the whole blood vessel, longitudinal cut, and lipid core are shown in Figs. 1A–C, respectively. The cross section of the vessel at the mid length of the artery is shown in Fig. 1D. The fibrous cap (FC), in this model is a 0.1mm thick tissue layer located between the lumen and the LC of the FA (Fig. 1D). The FC also contains either 1 or 2 spherical μCalc(s) at the center of the cap aligned in the circumferential direction, as shown in Figure 2. The diameter of the Calcs was 10 μm and the spacing between the μCalcs was 4 μm. The degree of stenosis in the FA model was defined as the ratio between the cross section area at the location of minimal radius in the FA and the cross section area in the healthy region of the vessel, in this model being 60.9%, which corresponds to a mildly severe stenotic FA.

Constitutive model

The soft tissue layers of the artery were treated as hyperelastic solid materials and its mechanical behavior under large strains was investigated using three different constitutive models, namely the Neo-Hookean, Mooney-Rivlin and Holzapfel models (Holzapfel et al., 2000; Holzapfel et al., 2005; Belzacq et al., 2012).

Neo-Hookean model (NH)—The strain energy density function in a compressible neo-Hookean material is given by

$$\psi = C_{10}(\bar{I}_1 - 3) + D_1(J-1)^2, \quad (1)$$

where C_{10} and D_1 are material constants related to the shear modulus, μ, and bulk modulus, K, of the tissue by

$$C_{10} = \frac{\mu}{2}, D_1 = \frac{K}{2}, \quad (2)$$

and $\bar{I}_1$, the first invariant of the deviatoric part of the right Cauchy-Green deformation tensor, is expressed as

$$\bar{I}_1 = J^{-2/3} I_1, \quad (3)$$

in which I_1 is the first invariant of the right Cauchy-Green deformation tensor, given by

$$I_1 = \lambda_1^2 + \lambda_2^2 + \lambda_3^2, \quad (4)$$

where λ_i are the principal stretches, and J is the third invariant of the deformation gradient, $\mathbf{F}$,

$$J=\det(\mathbf{F})=\lambda_1\lambda_2\lambda_3. \quad (5)$$

When the material is incompressible, $J = 1$ and the stress energy density function for an incompressible Neo-Hookean material becomes

$$\psi=C_{10}(I_1-3). \quad (6)$$

Mooney-Rivlin model (MR)—The strain energy density function in the Mooney-Rivlin model is a linear combination of the two first invariants of the left Cauchy-Green deformation tensor. The strain energy density function for a compressible Mooney-Rivlin solid material is given by:

$$\psi=C_{10}(\bar{I}_1-3)+C_{01}(\bar{I}_2-3)+D_1(J-1)^2 \quad (7)$$

where C_{10} and C_{01} are material constants, given by

$$C_{01}+C_{10}=\frac{\mu}{2}, D_1=\frac{K}{2}, \quad (8)$$

and $\bar{I}_1$ and $\bar{I}_2$ are defined as:

$$\begin{array}{ll}\bar{I}_1=J^{-2/3}I_1, & I_1=\lambda_1^2+\lambda_2^2+\lambda_3^2, J=\det(\mathbf{F}) \\ \bar{I}_2=J^{-4/3}I_2, & I_2=\lambda_1^2\lambda_2^2+\lambda_2^2\lambda_3^2+\lambda_3^2\lambda_1^2\end{array} . \quad (9)$$

In an incompressible Mooney-Rivlin solid material, $J = 1$, and the strain energy density function reduces to

$$\psi=C_{10}(\bar{I}_1-3)+C_{01}(\bar{I}_2-3). \quad (10)$$

Holzapfel model (H)—The strain energy density function in the Holzapfel solid material is given by (Holzapfel et al., 2000; Belzacq et al., 2012):

$$\psi=C_{10}(\bar{I}_1-3)+\frac{k_1}{2k_2}\sum_{\alpha=1}\left\{\exp\left[k_2\left[\kappa(\bar{I}_1-3)+(1-3\kappa)(\bar{I}_{4(\alpha\alpha)}-1)\right]^2-1\right]\right\}+D_1\left(\frac{J^2-1}{2}-\ln J\right) \quad (11)$$

where C_{10}, is associated to the non-collagenous matrix of the artery, and it describes the isotropic behavior of the material. The anisotropic behavior is thus taken into consideration by the constants k_1, and k_2. The collagenous fibers in each of the artery layers are arranged at a particular angle, which is described in a cylindrical polar coordinate system by

$$A=\begin{bmatrix}0\\ \cos\beta_i\\ \sin\beta_i\end{bmatrix} \text{and} A'=\begin{bmatrix}0\\ \cos\beta_i\\ -\sin\beta_i\end{bmatrix}, i=\mathrm{I,M,A} \quad (12)$$

where β_i are the angles between the collagen fibers, arranged in symmetrical spirals, in each of the artery layers, i = I, M, A. The parameter κ indicates the level of dispersion in the fiber direction.

Material properties

Parameters for the hyperelastic constitutive models, C_{10}, C_{01}, D_1, k_1, k_2, and β, were obtained from data (Mean ± SD) previously reported in the literature for each tissue layer (Holzapfel et al., 2005) and Eqs 2 & 7 (summarized in Table 1). In turn, the μCalcs are considered as homogeneous, isotropic, solid elastic material, with properties similar to calcified bone tissue, E= 18,000 kPa and ν=0.3. The lipid in the core is assumed as a homogeneous fluid with a 5kPa bulk modulus and ν=0.49.

3D Multiscale Finite Element Analysis

To obtain a detailed analysis of the stresses around the μCalcs in the cap of the fibroatheroma, a 3D sub-modeling approach was implemented (Maldonado et al., 2012; Maldonado et al., 2013) using ABAQUS (V. 6.10 Simulia, Providence, RI). The macroscopic scale or global model consists of the model geometry shown in Fig. 2A, which does not include the microcalcifications in the cap of the FA. A physiological level blood pressure of 110 mmHg (14.6 kPa) was applied at the lumenal side of the intima layer, and both displacement and rotation of nodes along the external surface of the adventitia were set to zero as boundary conditions of the global model.

Solution of this global model is then interpolated onto the boundary of the second level model, consisting of an annular section of the artery at the medial portion of the FA (Fig. 2B). The element size of the mesh in this second level model is ~10 times smaller than in the global model of the artery, producing a higher resolution of the stresses in the FA cap.

The solution on this annular section of the atheroma is then used to drive the third scale of the model, which consist of an arc segment of the cap at the center of the fibroatheroma (Fig. 2C). Inside this cap segment, a cylindrical region of interest (ROI) was meshed with finite elements about 10 times smaller than in the previous level. Two spherical μCalcs in close proximity to each other were introduced in the cylindrical ROI, aligned in the circumferential (tensile) axis of the cap (Fig. 2D), with a element size mesh 2 times smaller than the one used in the cylindrical ROI. The multiscale modeling thus made it possible to accurately resolve the stresses around the μCalcs.

The blood pressure applied to the lumen of the artery produces a significant increase in the stresses along the tensile axis of the fibrous cap (circumferential stresses, $\sigma_{\theta\theta}$), as shown for the pressurized condition of the first and second level models in Figs. 2E and 2F. At the third level model, it was also confirmed that the circumferential stress is the largest in the cap center, as shown in (Fig. 2G). A magnified view of the stresses around the μCalcs in the cap demonstrates that $\sigma_{\theta\theta}$ was greatly increased in the circumferential direction at the external poles of μCalcs and even more in the space between the μCalcs.

The circumferential stresses, $\sigma_{\theta\theta}$, are then measured at the nodes around the spherical μCalcs (Fig. 3) under two cases, first when the material properties of the spherical region

representing the μCalcs are substituted by those of the soft cap tissue ($\sigma_{\theta\theta}^{soft\ tissue}$, Fig. 3A) and second when the material properties of the μCalcs are those of calcified tissue ($\sigma_{\theta\theta}^{\mu Calc}$, Fig. 3B). The ratio between the circumferential stresses, $\sigma_{\theta\theta}^{\mu Calc}$ and $\sigma_{\theta\theta}^{soft\ tissue}$, is defined as a stress concentration factor (SCF) produced by the presence of μCalc(s) in the cap. For both measurements, the FE meshes were exactly the same and these measurements were obtained using the 3D multiscale modeling approach in which the blood pressure was applied to the lumen of the artery.

FE model convergence criteria

Convergence of the numerical solution of the model was investigated for all three scales in the model (whole FA, FA annular segment, and cap). Size of the finite elements used in each model was reduced until a change smaller than 0.5% in the circumferential stresses measured in the cap was reached. The mesh size for the several components of the model are reported in table 2. Each level of the multiscale models contained ~300,000–700,000 elements.

Patient-specific Fibroatheromas

Ninety six human coronary arteries were harvested from 32 atherosclerotic whole human hearts obtained from the National Disease Research Interchange. Both left and right coronary arteries were dissected preserving their ostium and segments from the right coronary artery (RCA), the left anterior descending artery (LAD) and the circumflex artery (LCX). Coronary specimens were scanned using a high resolution micro computed tomography (HR-μCT) system (1172, SkyScan, Belgium) at 6.7-μm resolution to identify the location of atheromas within the vessel, and thus re-scanned at 2.1-μm resolution for quantitative analysis of μCalcs in the atheroma. Water, air and hydroxyapatite standards (1mm diameter rods containing 250 and 750mg/cm^3 hydroxyapatite) were used to calibrate grey color images to mineral density (CTAn, V.1.10.1, SkyScan, BE), allowing identification of lipid, calcified and soft tissues within the atheroma. Sixty-six human coronary fibroatheromas were identified based on the presence of an eccentric thick vessel wall with a visible atheroma core. Histology and transmission electron microscopy (TEM) images of μCalcs found in human atheroma caps (Kelly-Arnold et al., 2013) were manually segmented and the 2D contours of the μCalc were approximated with overlapping ellipses of different size and aspect ratio. The ellipses were then revolved along their major axis to construct a 3D shape. This realistic complex 3D μCalc geometry was then placed virtually in the center of the cap of a 3D idealized atheroma.

μCalc aspect ratio

HR-μCT images of the atheromas were binarized to segment the calcified particles from the soft tissues in the atheroma using a global thresholding method (Gu et al., 2012; Palacio-Mancheno PE et al., 2013). The volume, surface and centroid of each individual 3D object was calculated automatically using CTAn analysis software. An equivalent spherical diameter $D = (6V/\pi)^{1/3}$ was calculated based on the volume V of each particle along with its sphericity S_{ph}, which is defined by $S_{ph} = S_{eq}/S$ where S is the measured surface area and $S_{eq} = \pi D^2$. If the particle is assumed to be an ellipsoid of revolution its sphericity can be

approximated by $S_{ph} = (r/l)^{1/3}$ provided $S_{ph} > 0.5$ or $l < 8r$. Using the volume of an ellipsoid, $V_{ell} = \pi r^2 l/6$ one can now solve for r and l, the semi-minor and semi-major axes of the ellipsoid. The aspect ratio of each μCalc was determined as l/r.

Simplified model to approximate complex μCalc boundary shapes

Simplified FEA models were used to investigate the effect of complex boundary shapes of agglomerated μCalcs on SCF at the poles of the μCalcs. An agglomerated particle from histology was approximated using (1) a simplified geometry in which the particle is formed by the tips at both ends of the particle, maintaining the same radii of curvature at its poles, (2) an equivalent ellipsoid with same major and minor axes as the particle, without maintaining the μCalc radii of curvature at the poles, (3) a model geometry with same major-axis length and radii of curvature at the poles of the μCalc.

Orientation of μCalc(s) relative to tensile axis of cap

The effect of the orientation of μCalcs relative to the tensile axis of the cap on the SCF at the poles of the inclusion was determined using FEA in two cases: (1) an elongated calcified particle, and (2) a pair of spherical μCalcs, after rotating the μCalc(s) clockwise every 10 degrees from 0° to 90° with respect of the tensile axis of the cap.

RESULTS

I. Effect of tissue properties on SCF around μCalcs

The effect of soft tissue shear modulus on the stress concentration factor created around μCalcs was determined using the 3D FEA multiscale approach in the compressible Neo-Hookean material model. The FEA was performed for 6 different values of μ (Mean−SD, Mean, Mean+SD, 5×Mean, 50×Mean and 100×Mean.) in each of the three main artery layers in Table 1, while keeping K and all other properties constant. The ratio between the peak circumferential stresses, $\sigma_{\theta\theta}^{\mu Calc}$ and $\sigma_{\theta\theta}^{soft\ tissue}$ at the surface of the μCalc was used to determine the SCF for each case. Comparison of the stress concentration factor for these 6 cases shown in Fig. 4 indicates that there is practically no difference between the SCF produced within the limits of variance for healthy arteries (Mean±SD), but it starts to decrease when μ becomes 5×Mean, and even more for 50×Mean and 100×Mean of healthy tissue shear modulus values. Five times the shear modulus seems to correspond to fibrotic tissue in the cap, while 50 and 100 times the shear modulus is here computed to confirm the observed trend, in which the SCF decreases as μ increases (i.e. the tissue stiffens).

II. Effect of tissue incompressibility on stress concentration factor around μCalcs

The effect of soft tissue compressibility, K, on the stress concentration factor created around μCalcs was determined using a similar approach to the one for the shear modulus above. In this case, all material parameters were kept constant, except for the value of K, which was varied as 1×Mean, 10×Mean, 100×Mean and 1000×Mean of the bulk compressibility modulus in all three artery layers from healthy tissue in Table 1. The corresponding Poisson's ratio, ν, for each of those values of K and μ was obtained using

$$\nu = \frac{3K/\mu - 2}{6K/\mu + 2}, \quad (13)$$

leading to $\nu_I^{1\times K} = 0.4488, \nu_M^{1\times K} = 0.4776, \nu_A^{1\times K} = 0.4040$ for the I, M and A layers under the 1×K condition; $\nu_I^{10\times K} = 0.4947, \nu_M^{10\times K} = 0.4977, \nu_A^{10\times K} = 0.4898$ for the 10×K case, and $\nu_I^{100\times K} = 0.4995, \nu_M^{100\times K} = 0.4998, \nu_A^{100\times K} = 0.4990$ for 100×K, and $\nu_I^{1000\times K} = 0.4999, \nu_M^{1000\times K} = 0.5000, \nu_A^{1000\times K} = 0.4999$ for 1000×K. Comparison of the SCF for these 4 cases of compressibility in Fig. 5 indicates that there is a very small difference between the SCF for 1×K and 10×K, but the decrease in SCF becomes significant at 100×K and 1000×K.

III. Effect of constitutive model on SCF around μCalcs

The effect of the constitutive model employed to calculate the peak circumferential stresses around μCalcs on the SCF was determined using the mean values of material properties reported in Table 1. The models that were compared include the isotropic compressible and incompressible Neo-Hookean, isotropic compressible and incompressible Mooney-Rivlin and the anisotropic compressible Holzapfel model. The SCF in the compressible case of the Neo-Hookean and Mooney-Rivlin models are practically the same. The incompressible case for both Neo-Hookean and Mooney-Rivlin also lead to SCF that are similar to each other, but significantly different to the compressible case. The anisotropic compressible Holzapfel model exhibited a SCF that is significantly smaller than the SCF obtained using isotropic compressible models, but larger than the SCF obatined for isotropic incompressible models (Figure 6).

IV. Effect of aspect ratio of μCalcs on SCF around μCalcs

The aspect ratio of elongated μCalcs was calculated as an equivalent prolate spheroid with an equivalent volume and surface area. Figure 7.A shows the average number of μCalcs as a function of their aspect ratio *l*/*r*. An average of 612±860 μCalcs have an *l*/*r*<2, 648±1091 μCalcs have 2<*l*/*r*<3, 261±450 μCalcs have 3<*l*/*r*<4, and 95±168 μCalcs have 4<*l*/*r*<8. Vengrenyuk et al. (2008) have shown that whereas a near spherical μCalc would cause a 2-fold increase in PCS, a prolate spheroid with an aspect ratio *l*/*r*>2 could cause more than a 4-fold increased stress in a localized region near its ends.

The aspect ratio and orientation of a single prolate μCalc along the tensile axis of the cap have an important effect on the SCF produced by such μCalc. A simplified FEA model was used to investigate the effect of complex boundary shapes of agglomerated μCalcs on SCF at the poles of the microinclusion. The histology-based FEA calculated stress concentration factor at the poles of the agglomerated particle in Kelly-Arnold et al., (2013) is shown in Figure 7.B and 7.C, indicating that the presence of this elongated particle would increase the local stress 4.2 times at its ends, instead of the 2-fold increase calculated for its volume equivalent sphere. In Figure 7.D, the agglomerated particle was approximated using a simplified geometry in which the particle is formed by the tips at both ends of the particle, maintaining the same radii of curvature at its poles, resulting in an underestimated SCF

(=2.9). On the contrary, when the agglomerated particle was approximated by an equivalent ellipsoid with same major and minor axes as the μCalc, without maintaining the particle radii of curvature at the poles, the SCF was significantly overestimated (SCF=7.6), as shown in Figure 7.E. The best result was found when the agglomerated particle was approximated by a simplified model that retained the length of the major axis of the particle and its curvature at the poles of the μCalc (SCF=4.3), as depicted in Figure 7.F.

V. Effect of orientation of μCalcs on SCF

The SCF also depends on the orientation of the elongated particle relative to the tensile axis of the cap. The SCF produced by the agglomerated calcification in Figure 7.B was analyzed at different orientations within the cap. The SCF was maximal when the particle was aligned with the tensile axis of the cap, and decreased to a minimum value when oriented perpendicular to the tensile axis, as shown in Figure 8.A, 8.C and 8.E. The orientation of two or more close particles, $h/D < 0.5$, (where h is the distance between particles and D the diameter of the particles) relative to the tensile axis of the cap can also have a directional-dependent effect on SCF. In Figure 8.B, 8.D and 8.F, the SCF is reported for a pair of spherical microinclusions (h/D=0.4) that were analyzed after being rotated every 10 degrees until being perpendicular to the tensile axis of the cap. The maximal PCS occurs between the pair of particles when oriented along the tensile axis. The PCS decreases as the particles are oriented off the tensile axis and becomes minimal (PCS=2) at the tensile poles of each particle, as if they were isolated one from the other. Interestingly, the SCF in the region located between the μCalcs is < 1.0 (value 0.5) indicating compression when they are found perpendicular to the tensile axis. Overall, the FEA indicates that four key shape parameters determine PCS at the poles of a single μCalc or pair of μCalcs: (1) the aspect ratio of the particle, (2) the curvature of the μCalc complex at its poles, (3) the proximity between μCalc pairs, and (4) the orientation of the μCalc(s) relative to the tensile axis of the cap.

DISCUSSION

In the present study, we investigated the effect of μCalcs on the peak circumferential stress within the cap of the fibroatheroma (FA) under a number of different material properties and hyperelastic constitutive models. We have found that the stress concentration factor (SCF) produced by the μCalcs in the FA cap is both affected by the material tissue properties, and the constitutive model employed. When the shear modulus of the three main layers in the artery was varied within the physiological range of healthy tissues, the SCF produced by μCalcs was practically the same. However, when the shear modulus increase 5 times, case corresponding to a fibrous cap tissue, the SCF slightly decreased, but decreased more significantly when the shear modulus increased 50–100 times the original value. The effect of the soft tissue compressibility on SCF was also analyzed by changing the value of the bulk modulus K, resulting in more noticeable changes in SCF, when compared to changes due to μ. Interestingly, the SCF decreased from almost 4 to less than 2 when a very high modulus (1000×K) was employed, for which case the soft tissues could be considered incompressible. When the SCF was studied using different constitutive models, similar results were found for both compressible Neo-Hookean and Mooney-Rivlin models, and also when comparing the incompressible cases for both these models. However the SCF in

the compressible and incompressible cases was significantly different. In turn, the anisotropic, compressible Holzapfel model produced SCF values smaller than the isotropic compressible Neo-Hookean and Mooney-Rivlin models, demonstrating an effect of anisotropy on SCF. Overall, these results indicate that both compressibility and anisotropy of the tissue play a role on the SCF produced by μCalcs. This is explained by the fact that the stress concentration factor depends on the contrast between the material properties inside and outside of the μCalcs, and it is in particular observed for the incompressible materials.

In addition to the contrast between soft and hard tissues in the cap, the μCalcs aspect ratio and their alignment relative to the tensile axis of the cap have an effect on the SCF produced by μCalcs. The SCF produced at the poles of a spherical particle in the cap has been shown to be 2, irrespective of its relative position in the cap (Vengrenyuk et al., 2006). However, an elongated particle in the cap would produce an SCF between 2–5 depending on its aspect ratio (Vengrenyuk et al., 2008). The studies by Maldonado et al., (2012; 2013) also provided the initial evidence that both the size of a μCalc and the proximity between pairs of μCalcs are important determinants of SCF in atheroma caps, and can potentially transform a stable plaque into a vulnerable one. The proximity, *h/D* ratio between two particles was confirmed to have an SCF between 2–7 in Kelly-Arnold, A. et al., (2013). In the present study, HR-μCT at 2.1-μm resolution allowed not only a more accurate quantification of the number of μCalcs, but assessment of their morphology (aspect ratio). It was shown that the μCalcs that produce a larger increase in SCF have an elongated shape and/or a small *h/D* ratio, when oriented along the tensile axis of the cap. While these findings are here reported for human coronary arteries containing microcalcifications, the calcification process is not exclusive to coronary arteries, and could happen in other arteries, such as carotid and iliac plaques. However, the background stresses generated in caps may be different since tissue composition, material properties and morphology of plaques in other blood vessels could be different.

The overall effect of microcalcifications in plaque vulnerability can be summarized as an intensifier of the background circumferential stress in the cap. The stress concentration factor (SCF) produced by μCalcs does not depend on the specific μCalc location within the cap (center or shoulders); it is now known that it depends on the properties of the soft tissue material in the artery layers, the compressibility of the tissue, its anisotropy, size and shape of the μCalc as well as the proximity between two or more μCalcs. The SCF, which is typically in the range of 2–5, can exceed five or more if the μCalcs are very closely spaced and aligned along the tensile axis of the cap. In turn, the magnitude of the background stress in the cap depends on the atheroma morphology (i.e. cap thickness, necrotic core size, location and shape of lipid core) and tissue composition (i.e. lipid core composition, residual stresses). Therefore, if the cap has no μCalcs, the cap needs to thin to ~30μm to reach the rupture threshold and become prone to rupture (Maldonado et al., 2012). Also, if μCalc(s) are located in caps with very low background stress, the increase in stress concentration produced by μCalcs may not be sufficient to reach the rupture threshold. However, the presence of μCalc(s) in the cap with a background stress of about one fifth - one half the rupture threshold (a stable plaque), will produce a significant increase on local stress, which

may exceed the cap rupture threshold, and thus transform a non vulnerable plaque into a vulnerable one.

Acknowledgments

This research has been supported by NIH ARRA grant RCI HL101151 to SW, NIH AG034198 to LC, NSF-BMMB 1333560, NSF-MRI 0723027, MRI 1229449 and PSC CUNY award to LC.

References

Akyildiz AC, Speelman L, van Brummelen H, Gutierrez MA, Virmani R, van der Lugt A, van der Steen AF, Wentzel JJ, Gijsen FJ. Effects of intima stiffness and plaque morphology on peak cap stress. Biomed Eng Online. 2011; 10:25. [PubMed: 21477277]

Belzacq T, Avril S, Leriche E, Delache A. A numerical parametric study of the mechanical action of pulsatile blood flow onto axisymmetric stenosed arteries. Med Eng Phys. 2012; 34(10):1483–1495. [PubMed: 22464939]

Born, GVR.; Richardson, PD. Mechanical properties of human atherosclerotic lesions. In: Glagov, S.; Newman, WP.; Shaffer, S., editors. Pathology of the Human Atherosclerotic Plaque. Berlin: Springer; 1989.

Burke AP, Farb A, Malcom GT, Liang Y, Smialek JE, Virmani R. Plaque rupture and sudden death related to exertion in men with coronary artery disease. JAMA. 1999; 281(10):921–926. [PubMed: 10078489]

Burke AP, Farb A, Malcom GT, Liang YH, Smialek J, Virmani R. Coronary risk factors and plaque morphology in men with coronary disease who died suddenly. N Engl J Med. 1997; 336(18):1276–1282. [PubMed: 9113930]

Cardoso L, Weinbaum S. Changing views of the biomechanics of vulnerable plaque rupture: a review. Ann. Biomed. Eng. Published online: 11 July 2013.

Cheng GC, Loree HM, Kamm RD, Fishbein MC, Lee RT. Distribution of circumferential stress in ruptured and stable atherosclerotic lesions. A structural analysis with histopathological correlation. Circulation. 1993; 87(4):1179–1187. [PubMed: 8462145]

Davies MJ, Thomas AC. Plaque fissuring--the cause of acute myocardial infarction, sudden ischaemic death, and crescendo angina. Br Heart J. 1985; 53(4):363–373. [PubMed: 3885978]

Davies MJ, Thomas T. The pathological basis and microanatomy of occlusive thrombus formation in human coronary arteries. Philos Trans R Soc Lond B Biol Sci. 1981; 294(1072):225–229. [PubMed: 6117886]

Finet G, Ohayon J, Rioufol G. Biomechanical interaction between cap thickness, lipid core composition and blood pressure in vulnerable coronary plaque: impact on stability or instability. Coron Artery Dis. 2004; 15(1):13–20. [PubMed: 15201616]

Gu XI, Palacio-Mancheno PE, Leong DJ, Borisov YA, Williams E, Maldonado N, Laudier D, Majeska RJ, Schaffler MB, Sun HB, Cardoso L. High resolution micro arthrography of hard and soft tissues in a murine model. Osteoarthritis and Cartilage. 2012; 20(9):1011–1019. [PubMed: 22613702]

Holzapfel GA, Gasser TC, Ogden RW. A new constitutive framework for arterial wall mechanics and a comparative study of material models. Journal of Elasticity. 2000; 61(1–3):1–48.

Holzapfel GA, Sommer G, Gasser CT, Regitnig P. Determination of layer-specific mechanical properties of human coronary arteries with nonatherosclerotic intimal thickening and related constitutive modeling. Am J Physiol Heart Circ Physiol. 2005; 289(5):H2048–H2058. [PubMed: 16006541]

Kelly-Arnold A, Maldonado N, Laudier D, Aikawa E, Cardoso L, Weinbaum S. A revised microcalcification hypothesis for fibrous cap rupture in human coronary arteries. Proc Natl Acad Sci USA. 2013; 110(26):10741–10746. [PubMed: 23733926]

Maehara A, et al. Morphologic and angiographic features of coronary plaque rupture detected by intravascular ultrasound. J. Am. Coll. Cardiol. 2002; 40(5):904–910. [PubMed: 12225714]

Maldonado N, Kelly-Arnold A, Cardoso L, Weinbaum S. The explosive growth of small voids in vulnerable cap rupture; cavitation and interfacial debonding. J Biomech. 2013; 46(2):396–401. [PubMed: 23218838]

Maldonado N, Kelly-Arnold A, Vengrenyuk Y, Laudier D, Fallon JT, Virmani R, Cardoso L, Weinbaum S. A mechanistic analysis of the role of microcalcifications in atherosclerotic plaque stability: potential implications for plaque rupture. Am J Physiol Heart Circ Physiol. 2012; 303(5):H619–H628. [PubMed: 22777419]

Palacio-Mancheno PE, Larriera AI, Doty SB, Cardoso L, SP F. 3D assessment of cortical bone porosity and tissue mineral density using high- resolution micro-CT: effects of resolution and threshold method. J. Bone Miner. Res. 2014 Jan; 29(1):142–150. [PubMed: 23775635]

Rambhia SH, Liang X, Xenos M, Alemu Y, Maldonado N, Kelly A, Chakraborti S, Weinbaum S, Cardoso L, Einav S, Bluestein D. Microcalcifications increase coronary vulnerable plaque rupture potential: a patient-based micro-CT fluid-structure interaction study. Ann Biomed Eng. 2012; 40(7):1443–1454. [PubMed: 22234864]

Richardson PD, Davies MJ, Born GV. Influence of plaque configuration and stress distribution on fissuring of coronary atherosclerotic plaques. Lancet. 1989; 2(8669):941–944. [PubMed: 2571862]

Speelman L, Akyildiz AC, den Adel B, Wentzel JJ, van der Steen AF, Virmani R, van der Weerd L, Jukema JW, Poelmann RE, van Brummelen EH, Gijsen FJ. Initial stress in biomechanical models of atherosclerotic plaques. J Biomech. 2011; 44(13):2376–2382. [PubMed: 21782179]

Tang D, Yang C, Zheng J, Woodard PK, Saffitz JE, Petruccelli JD, Sicard GA, Yuan C. Local maximal stress hypothesis and computational plaque vulnerability index for atherosclerotic plaque assessment. Ann Biomed Eng. 2005; 33(12):1789–1801. [PubMed: 16389527]

Vengrenyuk Y, Cardoso L, Weinbaum S. Micro-CT based analysis of a new paradigm for vulnerable plaque rupture: cellular microcalcifications in fibrous caps. Mol Cell Biomech. 2008; 5(1):37–47. [PubMed: 18524245]

Vengrenyuk Y, Carlier S, Xanthos S, Cardoso L, Ganatos P, Virmani R, Einav S, Gilchrist L, Weinbaum S. A hypothesis for vulnerable plaque rupture due to stress-induced debonding around cellular microcalcifications in thin fibrous caps. Proc Natl Acad Sci U S A. 2006; 103(40):14678–14683. [PubMed: 17003118]

Vengrenyuk Y, Kaplan TJ, Cardoso L, Randolph GJ, Weinbaum S. Computational Stress Analysis of Atherosclerotic Plaques in ApoE Knockout Mice. Annals of Biomedical Engineering. 2010; 38(3): 738–747. [PubMed: 20336835]

Virmani R, Burke AP, Kolodgie FD, Farb A. Pathology of the thin-cap fibroatheroma: a type of vulnerable plaque. J Interv Cardiol. 2003; 16(3):267–272. [PubMed: 12800406]

Virmani, R.; Narula, J.; Leon, M.; Willerson, JTE. The Vulnerable Atherosclerotic Plaque: Strategies for Diagnosis and Management. Malden, MA: Blackwell; 2007.

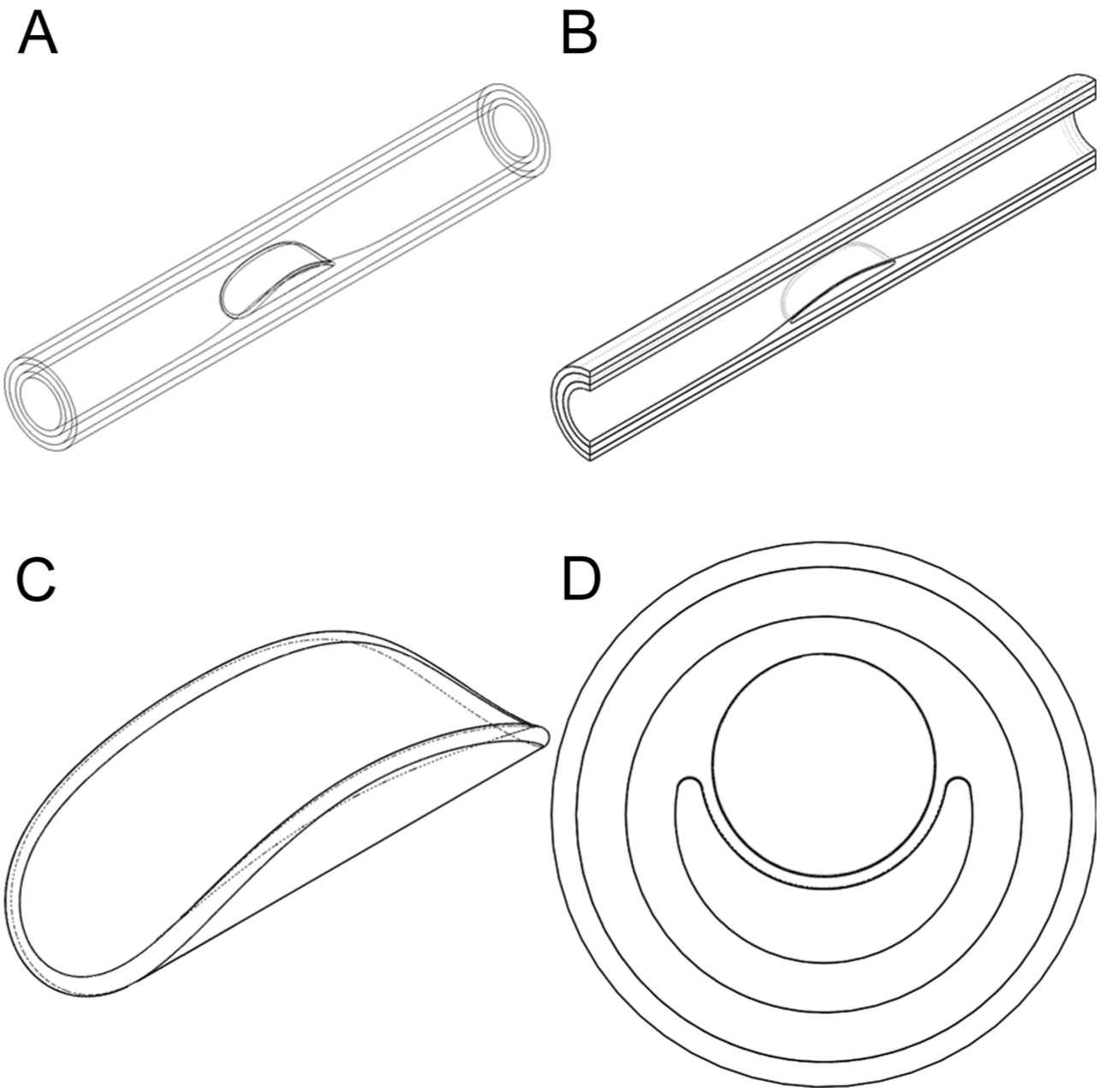

Figure 1.
Idealized macroscopic model of a human coronary fibroatheroma. A) Isometric view of the whole blood vessel, B) longitudinal cut, C) lipid core, and D) cross section of the FA.

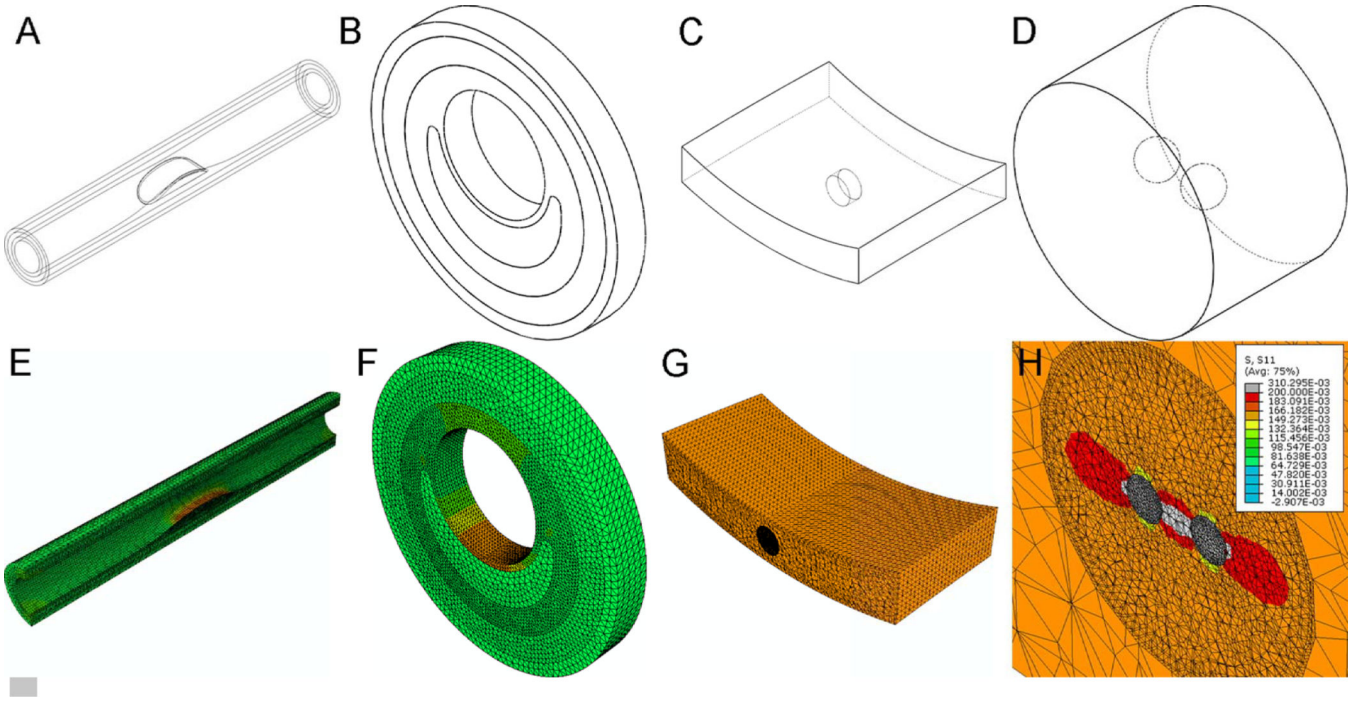

Figure 2.

Multiscale FEA approach to analyze circumferential stresses around μCalcs embeded in the cap of a fibroatheroma. **A**) macroscopic (global) model, **B**) annular section of the atheroma, **C**) microscopic model of the atheroma cap with μCalcs in the center of the cap, and **D**) magnified view of the cylindrical ROI containing two μCalcs aligned to the tensile axis of the cap. **E–H**) Map of circumferential stresses under the loaded condition for all three scales of modeling. **H**) $\sigma_{\theta\theta}$ was greatly increased in the circumferential direction at the external poles of μCalcs and even more in the region between the μCalcs, whose spacing was 0.4 times their diameter.

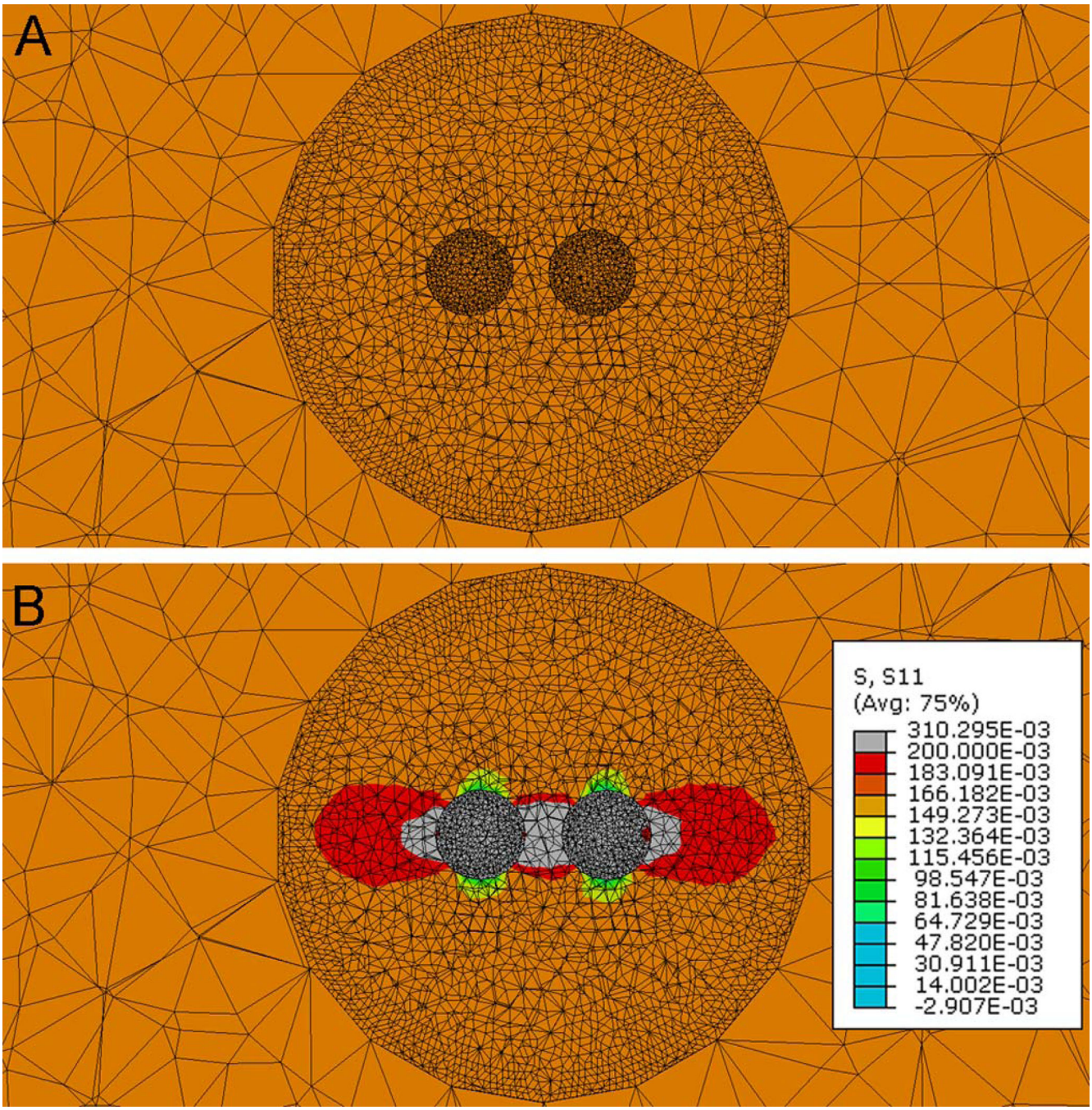

Figure 3.

The stress concentration factor is computed using the third level model under the loaded condition, in which the material properties of the μCalcs are either those of the intima fibrotic tissue (Fig. 3A) or those of calcified tissue (Fig. 3B). The SCF due to the presence of μCalcs is computed as the ratio of the circumferential stresses, $\sigma_{\theta\theta}^{\mu Calc}$ and $\sigma_{\theta\theta}^{soft\ tissue}$ at the tensile pole of the μCalc.

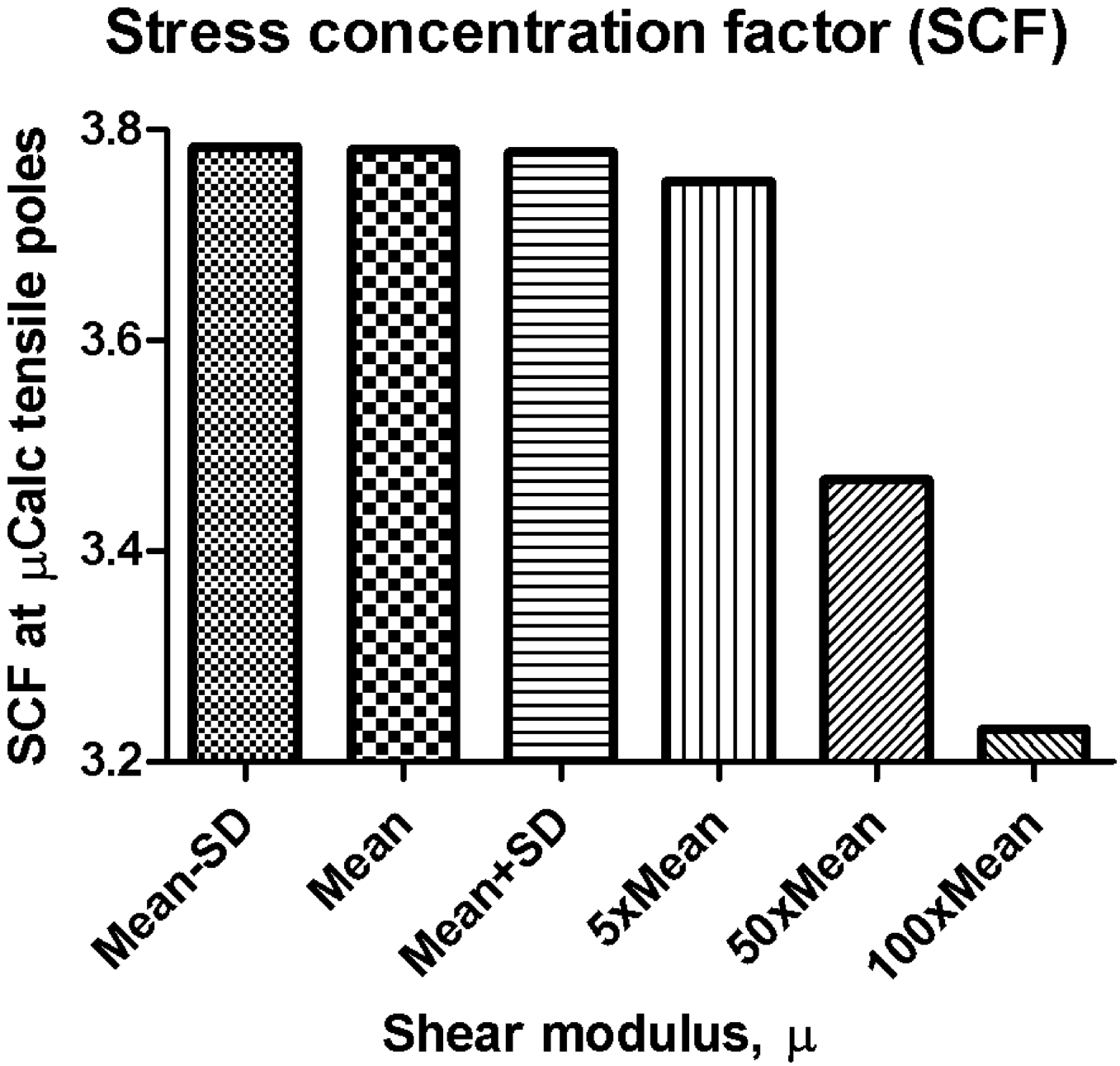

Figure 4.

Effect of tissue properties on stress concentration factor around μCalcs. Changes on SCF are shown as a function of changes on material properties of all three main artery layers (Mean −SD, Mean, Mean+SD, 5×Mean, 50×Mean and 100×Mean). Isotropic Neo-Hookean hyperelastic constitutive model.

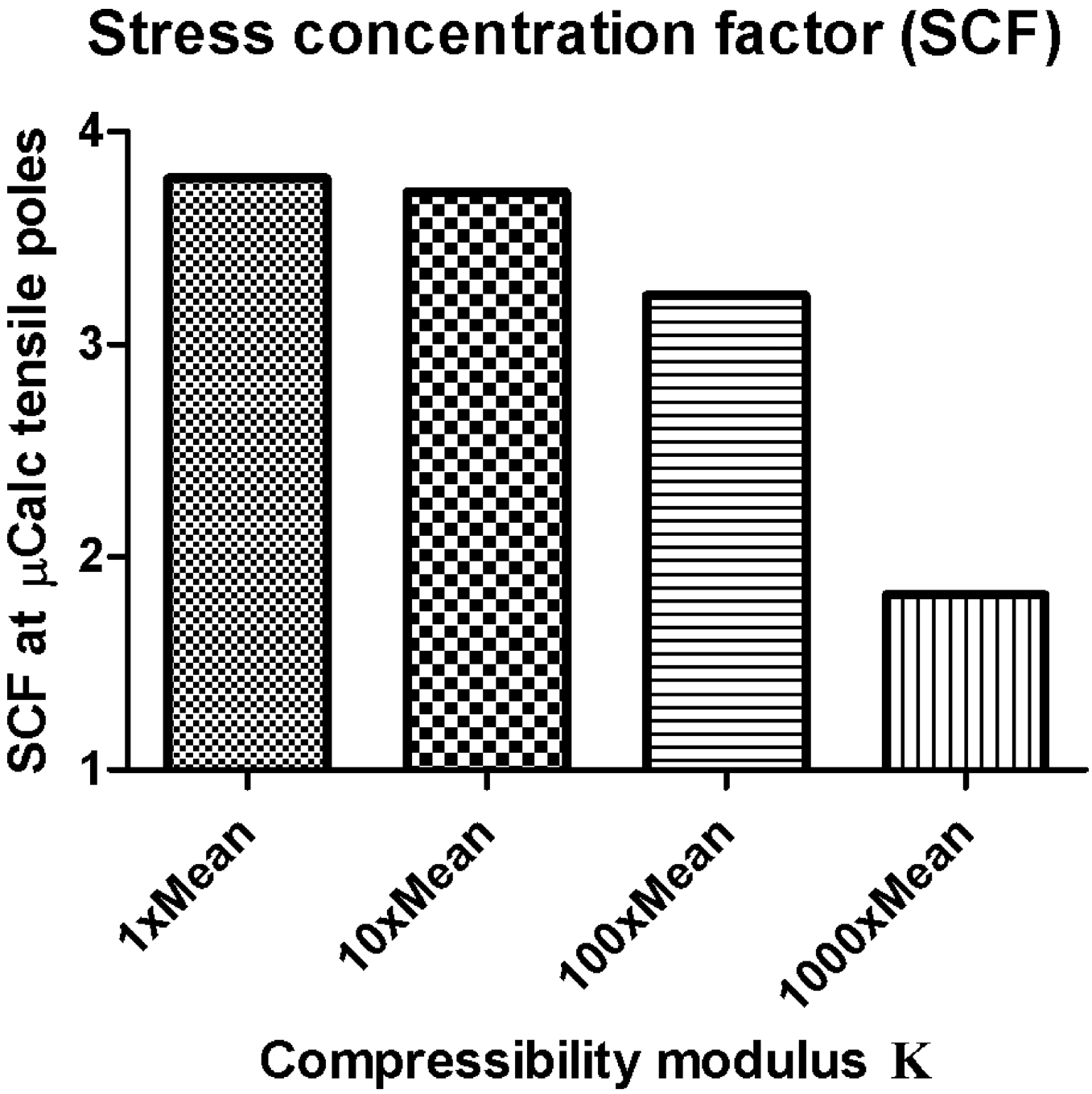

Figure 5.

Effect of tissue incompressibility on SCF around μCalcs. Changes on SCF are shown as a function of changes on bulk modulus (1×Mean, 10×Mean, 100×Mean and 1000×Mean) in all three main artery layers using values of μ and *K* in Table 1. Isotropic Neo-Hookean hyperelastic constitutive model.

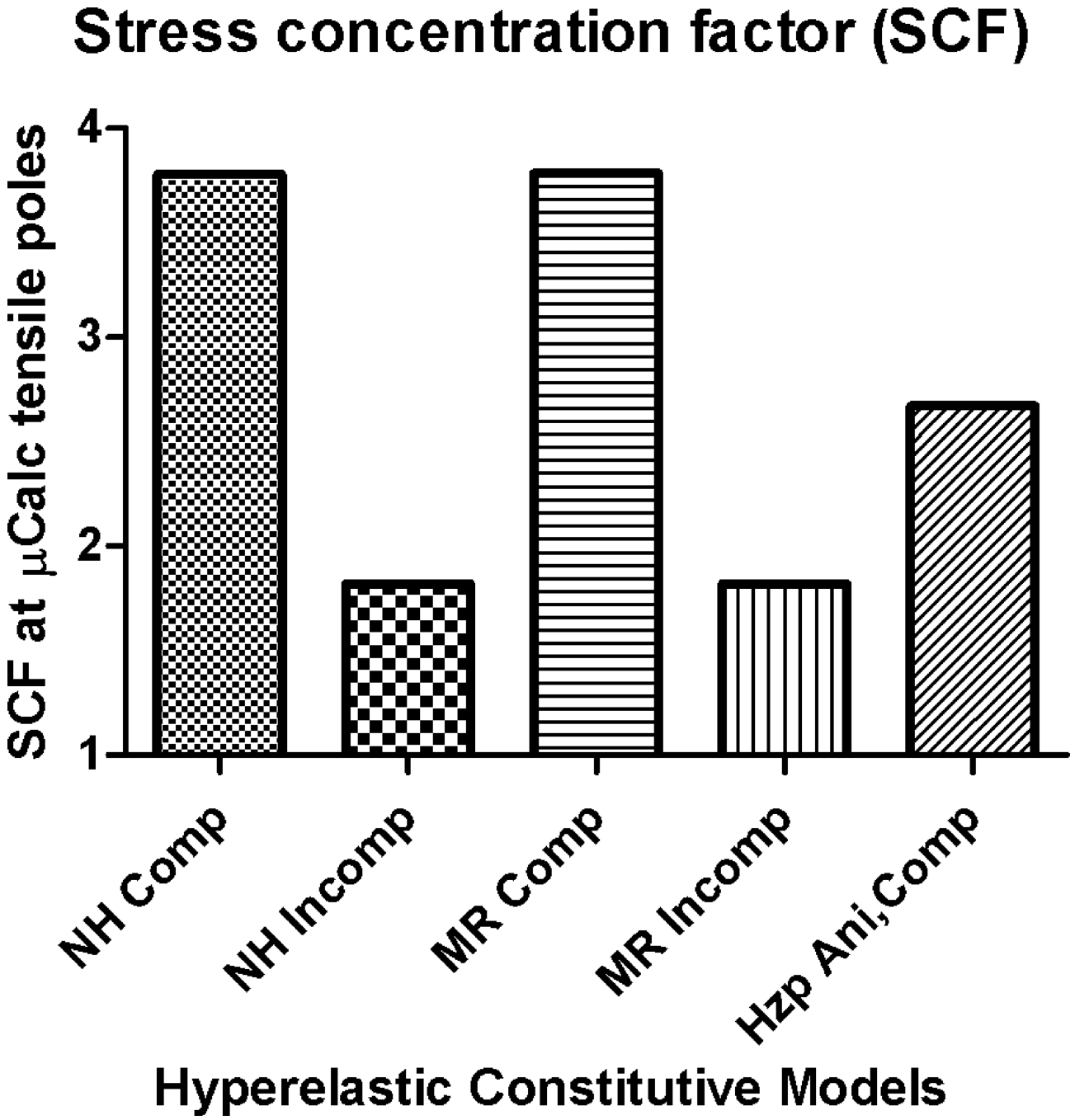

Figure 6.

Effect of hyperelastic constitutive model on stress concentration factor around μCalcs. A) Neo-Hookean compressible, B) Neo-Hookean incompressible, C) Mooney-Rivlin compressible, D) Mooney-Rivlin incompressible, and E) Holzapfel anisotropic compressible.

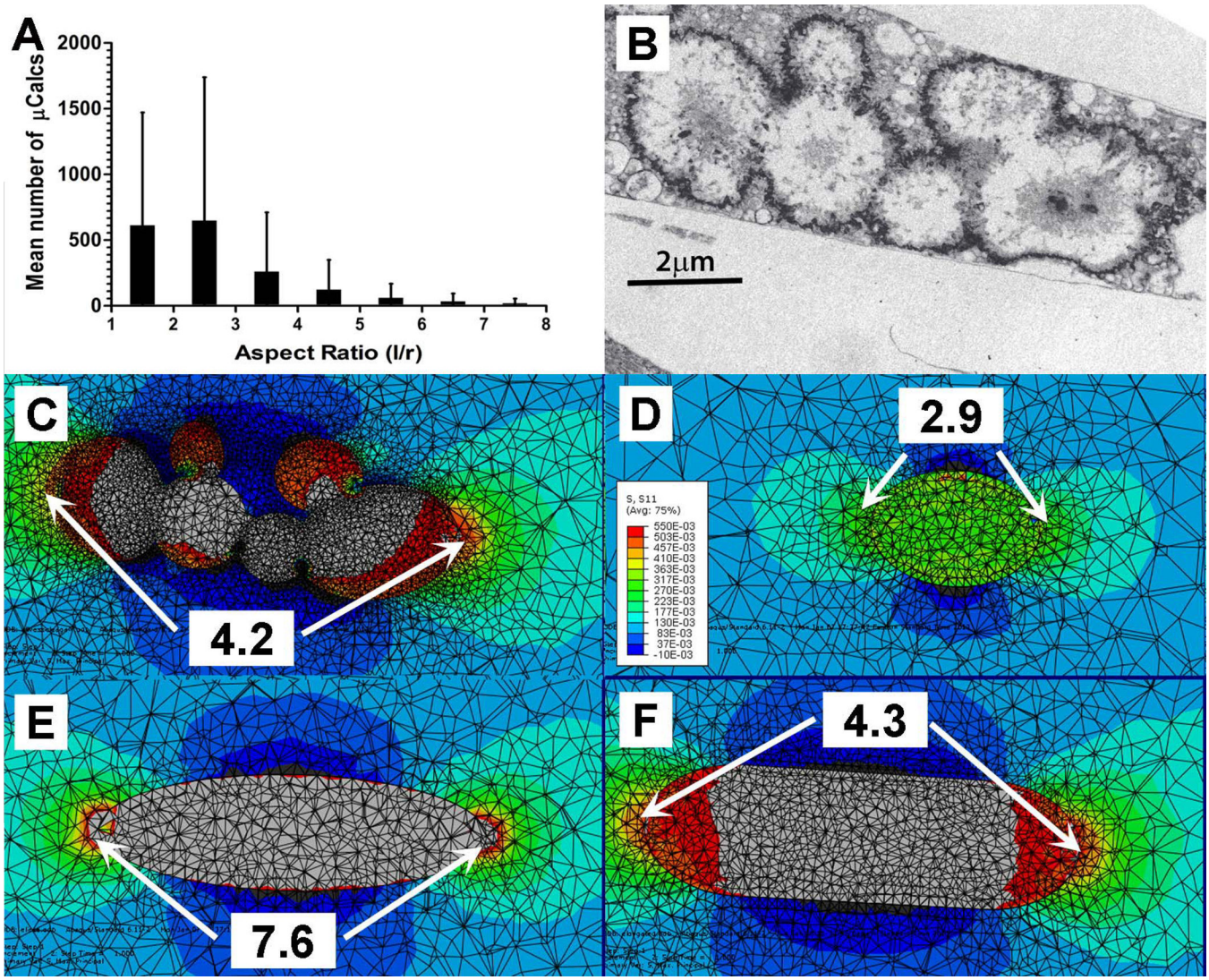

Figure 7.

Simplified FEA model was used to investigate the effect of complex boundary shapes of agglomerated μCalcs on SCF. (A) distribution of μCalcs in the fibrous cap by aspect ratio, (B) TEM image of aggregated calcifying matrix vesicles forming μCalcs in a mouse atheroma, (C) original boundary shapes of agglomerated μCalcs in panel B, (D) a simplified model geometry in which the radii of curvature at the poles were maintained, (E) an equivalent ellipsoid with same major and minor axes as the μCalc, but without maintaining the particle curvature at the poles, (F) same major length of the particle and its curvature at the poles of the μCalc. Numbers show calculated stress concentration factor at the poles.

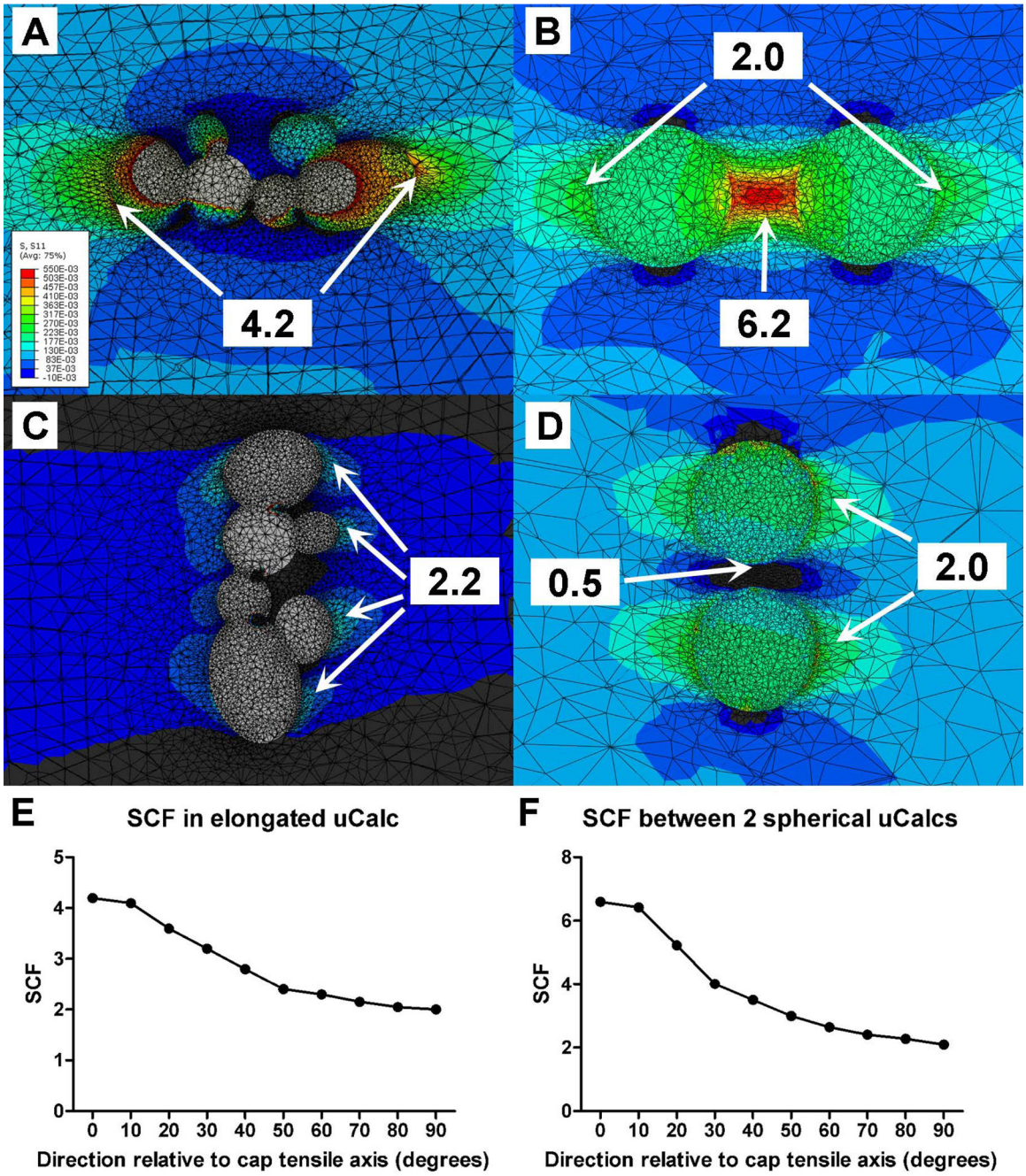

Figure 8.

Variations in stress concentration factor (SCF) due to the orientation of the Calc relative to the tensile axis of the cap. (A) SCF produced by the agglomerated calcification in Figure 7.B when oriented parallel to the tensile axis of the cap, and (C) oriented perpendicular to the tensile axis of the cap. (B) SCF due to a pair of two close particles, $h/D = 0.4$, (where h is the distance between particles and D the diameter of the particles) along the tensile axis of the cap, and (D) perpendicular to the tensile axis of the cap. SCF reported as a function of

the particle orientation relative to the tensile axis of the cap for particle agglomeration in (A), Fig. 8E, and spherical particle pair in (B), Fig. 8F.

Table 1

Material properties of intima, media and adventitia from Holzapfel, G. A. et al., (2005)

	μ (kPa)	K (kPa)	k_1 (kPa)	k_2 (---)	β (degrees)
Intima	27.90±10.59	130±250	263.66±490.95	170.88±125.47	60.3±18.2
Media	1.27±0.63	10±3.5	21.60±7.12	8.21±3.27	20.6±5.5
Adventitia	7.56±4.66	20±16	38.57±32.53	85.03±58.94	67.0±8.5

Table 2

Mesh size for the several components of the model

	Global model	Annular model	Arc segment of the cap		
			Cap segment	*Cylindrical ROI*	*μCalcs*
Intima	431,886	200,886	196,854	79,035	42,291
Media	111,524	116.845	---	---	---
Adventitia	135,591	66,848	---	---	---
Lipid core	44,355	42,401	---	---	---
TOTAL	**723,356**	**426,980**	**318,180**		